SLAC-TN-05-067

Measurement of gravitational lens time delays with LSST[1]

Lowry Anna Kirkby
Magdalen College, Oxford University, United Kingdom

Office of Science, Science Undergraduate Laboratory Internship (SULI)
Stanford Linear Accelerator Centre
Menlo Park, California

August 27, 2005

Prepared in partial fulfilment of the requirements of the Office of Science, Department of Energy's Science Undergraduate Laboratory Internship under the direction of Dr. Phil Marshall in the Kavli Institute for Particle Astrophysics and Cosmology (KIPAC) at the Stanford Linear Accelerator Center (SLAC), California.

Participant: ______________________________
Signature

Research Advisor: ______________________________
Signature

---

[1] Large Synoptic Survey Telescope

Work supported by Department of Energy contract DE-AC02-76SF00515

Abstract

The proposed Large Synoptic Survey Telescope will be the first to explore multiple dark energy probes simultaneously, including baryon acoustic oscillations, weak lensing, and strong gravitational lensing. The large data sample, covering the entire visible sky every few nights, will allow an unprecedented survey of deep supernova sources and their lensed images. The latter have not yet been observed. Notably, LSST will measure the *time delays* between different strong-lensed images of the same supernova. This will provide a unique probe of dark matter, dark energy, and the expansion rate of the Universe.

By simulating LSST observations under realistic conditions, we determined the time delay precision of multiple images from a representative strong-lensed Type Ia supernova. The output of the simulation was a set of light curves according to field and filter, which were subsequently analysed to determine the experimental time delays. We find that a time delay precision of better then 10% can be achieved under suitable conditions. Firstly, a minimum observed peak-magnitude of 22 is required for the lensed image, corresponding to an intrinsic source magnitude of about 24. The number of such supernova sources expected for LSST is under investigation, but it could amount to several thousand. Secondly, a minimum of about 50 visits per field is required, and, moreover, these visits must be evenly distributed over the duration of the event. The visit frequency should be approximately once per week, or better. Thirdly, the sky brightness should be below 21 magnitude arecsec^{-2} to allow sufficient sensitivity to distance sources.

Under the nominal LSST visiting schedule and field conditions, 15% of all fields satisfy these criteria, and allow time delay measurements of better than 10% precision. This performance can be further improved by fitting the predicted supernova light curves to the observations, rather than using the simple weighted mean as in the present study. Of the well-measured fields, 85% involve observations taken with the r filter, which has a wavelength acceptance that is well-matched to supernova spectra. This filter therefore represents the best choice for strong gravitational lens observations with LSST.

Our primary conclusion is that the visiting schedule is the single most important parameter to optimise for time delay measurements, and, once a lensed supernova has been detected, that frequent, regular observations should be scheduled to search with the highest sensitivity for multiple, delayed lensed images.

Contents

1 Introduction

1.1 The Large Synoptic Survey Telescope (LSST)

The proposed LSST is a ground-based telescope currently under study at Stanford Linear Accelerator Center (SLAC) [1]. The telescope is designed to have a large aperture, large field of view and high resolution (Table 1) in order to allow the entire observable sky to be mapped every few nights. Current telescopes either have a collection area large enough to produce deep images over a small field of view, or else can observe large areas of sky quickly but only to shallow depth. With its high etendue,[2] LSST will be able to capture the variation of short-lived stellar objects, such as exploding supernovae—effectively taking a movie of our dynamic Universe.

Table 1: Comparison between LSST and the Sloan Telescope. As a reference point, the field of view of the full moon is 0.5°.

Parameter		**LSST**	**Sloan**
Aperture	[m]	8.4	2.5
Field of view	[degrees]	3.5	2.5
CCD pixels	[$\times 10^9$]	3.0	0.1

Table 1 compares the performance of LSST with the current state-of-the-art sky survey, the Sloan Digital Sky Survey, at the Apache Point Observatory, New Mexico. The LSST is aiming for the deepest, fastest, widest and finest imaging ever achieved in one telescope. The images will be recorded using one of five colour filters (designated g, r, i, z and Y). These are weighted towards the red end of the spectrum in order to probe the farthest reaches of the Universe, where objects have a large redshift.

The primary goals of LSST are to explore the dark matter of the Universe, and to shed light on the nature of dark energy. At present, most dark matter and dark energy telescopes probe weak gravitational lensing, i.e. the coherent distortion of background sources, such as galaxies or galactic clusters. Weak lensing surveys are a central goal of LSST. However, LSST will open up a unique window on dark matter and dark energy by its ability to pursue multiple probes simultaneously, such as baryon acoustic oscillations and strong gravitational lensing.

1.2 Strong gravitational lensing

Gravitational lensing falls into three regimes: strong lensing, weak lensing and microlensing [2]. Strong lensing is characterised by the formation of multiple images of the source (e.g. the two images shown in Fig. 1). The lens typically consists of a galaxy, or galaxy cluster; the source may be a quasar, a supernova or a distant galaxy. Measurement of the image separation allows reconstruction of the lens's mass distribution, which provides information on its matter and dark matter content. If the lens has an asymmetric mass distribution, or if the source is not directly aligned with the lens (as in Fig. 1), the optical path lengths of the images differ. The arrival time of the light is a result both of geometry (the physical path length difference) and of gravitational effects. If the source is variable, as are quasars and supernovae, the images will also be variable and the time delays between images can be measured. Simultaneous measurement of the time delay and mass distribution allows Hubble's constant, H_0, to be determined, and thus provides a measure of the expansion rate of the Universe.

---

[2] *Etendue* is the cross-sectional area of a cone of light times the solid angle subtended by the light.

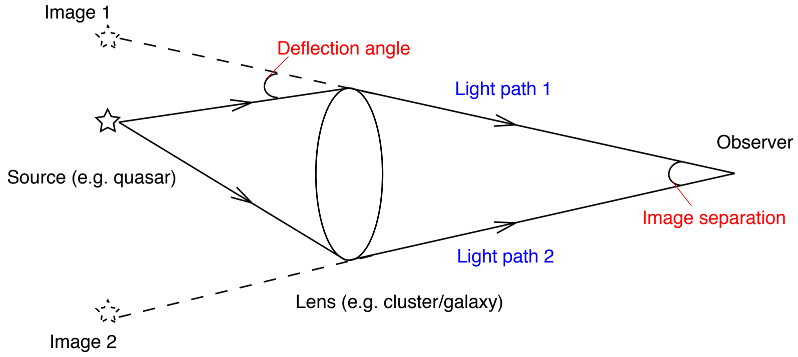

Figure 1: Strong gravitational lensing. Multiple images of the source are seen by the observer, as a result of the deflection of light due to the curvature of spacetime.

1.3 Aim of this study

The LSST is estimated to increase the strong-lens sample to at least 10,000 systems—an increase of about two orders of magnitude beyond present world statistics. In addition, LSST is expected to observe the first strong-lensed supernovae and, moreover, to collect a large event sample. Supernovae exhibit well-known light curves with a sharp rise and fall in brightness, providing precise time delay measurements. However, since the telescope will be scanning the sky, there will be gaps in the supernovae light curves, which may reduce the precision of the time delay measurement, and hence reduce the precision of the H_0 determination.

The diverse science goals of LSST involve different spatial, temporal and colour sampling requirements. An optimum observing strategy would maximise the science return from a single set of observations. The aim of our study is to investigate whether the proposed telescope design and operation strategy can deliver the required science from strong lensing surveys.

Our tests and results are described below. The first test involves estimating the threshold source magnitude required for good time delay measurements (§3.1), followed by tests involving the proposed observing strategy (§3.2). In the concluding section (§4), I will discuss the overall results, as well as suggest possible improvements in the observing strategy.

2 Experimental methods

2.1 LSST simulation

The operation of LSST is currently simulated by the *LSST Observation Simulator*[3]. The Simulator uses real seeing[4] and weather data, taken from the Cerro Tololo Inter-American Observatory (CTIO) [3] in Chile—a site with similar conditions to those proposed for LSST.

The Simulator is able to schedule observations based on a multitude of parameters, such as seeing, airmass, sky brightness, sun and moon angle; it also takes into consideration telescope parameters such as slewing time, shutter time and filter change time. The user is able to run the simulation for as long as desired, and to vary telescope parameters such as exposure time and exclusion zones. The output run history is stored in a MySQL database repository. For each observation, 34 attributes are stored. For this study, we extracted the telescope position

---

[3] Written by F. Pierfederici and K. Cook, National Optical Astronomy Observatory (NOAO), Tucson, Arizona.

[4] Astronomical *seeing* is the clarity with which the image is observed by a ground-based telescope, primarily determined by Earth's atmosphere. The seeing is the measured diameter (full width half maximum) of a point source (for example, a star) observed through the atmosphere. The best conditions (e.g. at the Magellan telescope, Chile) reach a minimum seeing of about 0.3–0.4 arcseconds.

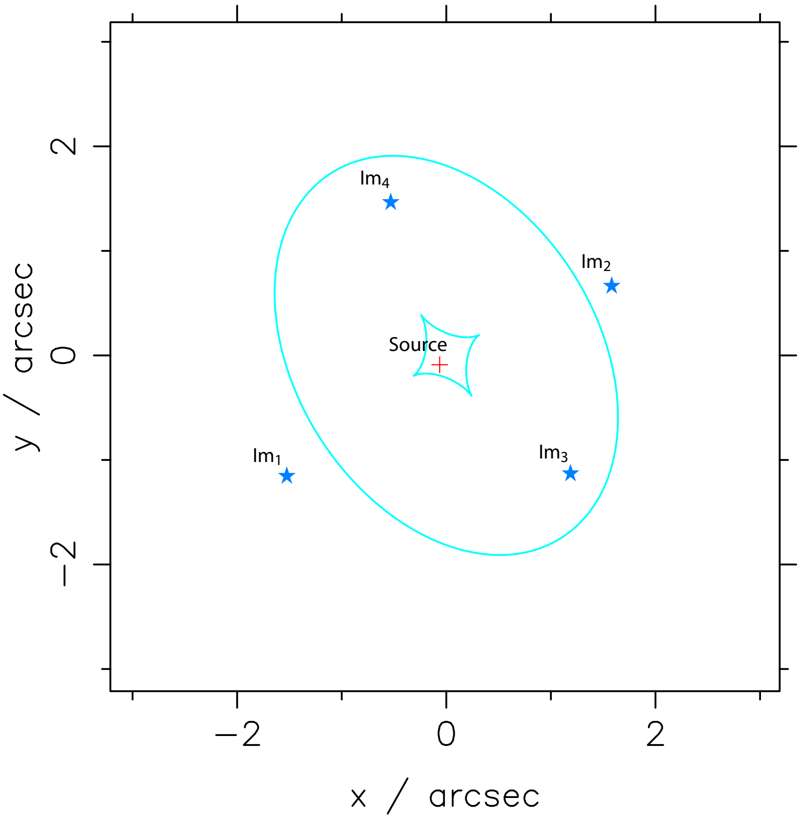

Figure 2: Schematic diagram of System LSN. The turquoise oval and caustic represent the projection of the critical curves in the lens plane (lines of critical density) onto the source plane. These are lines of infinite image magnification. The centre of the lens is positioned at (0, 0). The red cross indicates the position of the source (in this case a supernovae), and the four blue stars (labelled Im_1–Im_4) indicate the positions of the lensed images of the source.

(the LSST field observed), the filter, the seeing and the sky brightness. We ran the Simulator for an effective operational period of one year.

2.2 Generating a strong lens system

A simple mass model for elliptical galaxies and galactic clusters is the *Single Isothermal Ellipsoid* model, in which the density of matter falls off with the inverse of the square of the radius. We simulated a strong lens system using the modelling program *SIElens*,[5] which incorporates the Single Isothermal Ellipsoid mass model. Since strong lensed supernovae have not yet been observed, we modelled and investigated a fictitious system named *System LSN* (Lensed SuperNova).

2.2.1 Modelling System LSN

System LSN comprises a Type Ia supernova lensed by an elliptical galaxy, to form a quad image system. A schematic is shown in Fig. 2, and the parameters are summarised in Table 2. For the initial study described here, we designed System LSN to represent a relatively high quality system, with large image separations and long time delays between images (Table 3).

---

[5] Written by Phil Marshall, SLAC, Stanford, California.

Table 2: Lens and source parameters of System LSN.

System parameter		Value	
Lens:			
Position	θ_x, θ_y	0, 0	arcsec
Redshift	z_d	0.40	
Velocity dispersion	σ_v	350.0	km/s
Magnitude	m_d	17.68	
Effective radius	r_e	1.50	arcsec
Axis ratio	q	0.70	
Orientation	ϕ	-58.0	degrees
Source:			
Position	β_x, β_y	-0.06, -0.09	arcsec
Redshift	z_s	0.90	
Magnitude (unlensed)	m_s	25.5	

Table 3: Magnitude changes of the four lensed images, and time delays relative to Im_1.

Image	Magnitude change due to lensing	Time delay (days)
Im_1	-1.5	0.0
Im_2	-2.0	31.6
Im_3	-1.6	42.6
Im_4	-1.3	54.8

2.2.2 Light curve generation

We generated the system's four light curves[6] using an idealised, dense time sampling, as shown in Fig. 3a). The same light curves are shown Fig. 3b) assuming measurements with realistic LSST time sampling, using the LSST Observation Simulator. Both sets of light curves correspond to observations taken in the r filter only. Despite the sparser time sampling, LSST observes the four lensed images with well-resolved time delays and even retains the detailed shape of the supernovae light curves (notice, for example, that the break in the trailing edge is clearly detected).

2.3 Measuring the time delay precision

System LSN will have a distinct light curve in each LSST field as a result of the different visiting schedules per field. From these light curves and the weather conditions extracted from

---

[6] Using the *snlcsim* code written by Liz Rivers, Wellesley College, MA.

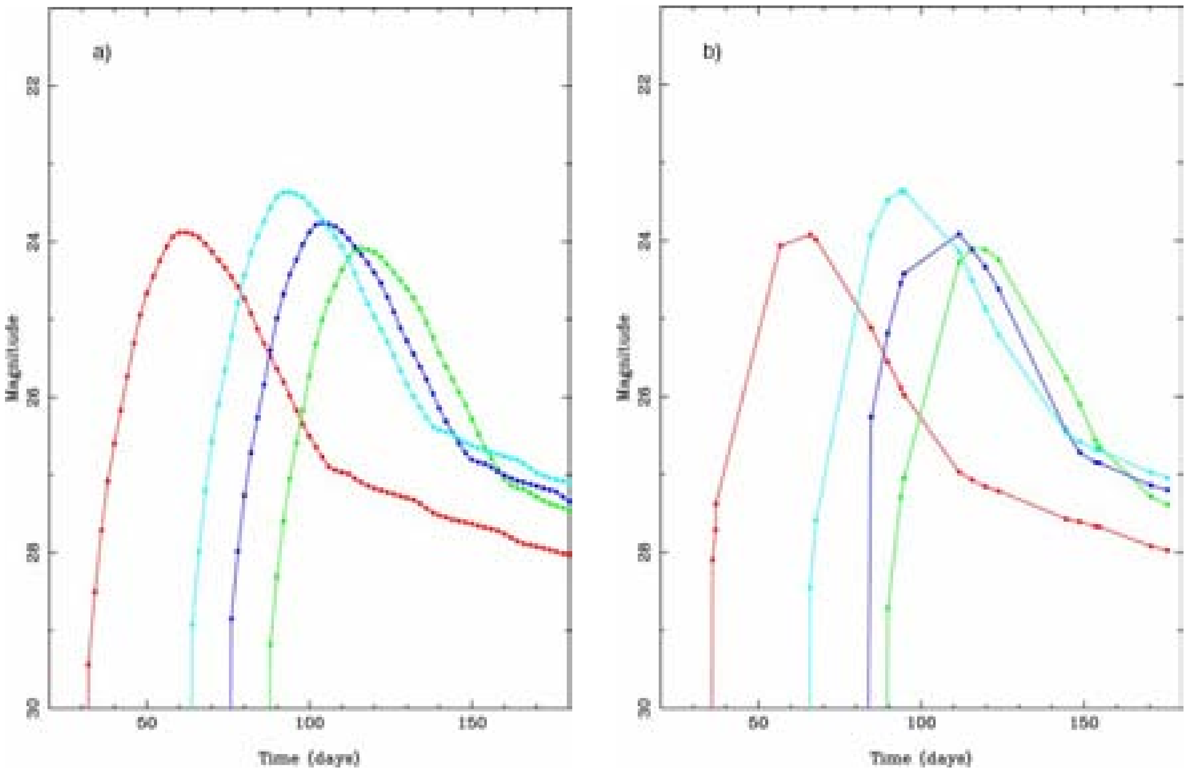

Figure 3: Light curves of System LSN in the r filter for a) an idealised, dense time sampling and b) a realistic time sampling with LSST. Each curve corresponds to a different lensed image of the supernova. The images are labelled 1 to 4 in order of time (red: 1, turquoise: 2, blue: 3, green: 4). The time delays are 32, 43 and 55 days between images 1–2, 1–3 and 1–4, respectively. Note that the intrinsic source magnitude is about 25.5; the brighter images result from the magnifications due to lensing.

the Observation Simulator, mock LSST images were generated[7] for each day of observation.

We modified the program to produce 4 "fits file" images for each observation day—one of each image in System LSN. We measured the flux and flux error of these images using the Source Extractor astronomical software tool, *SExtractor* [5]. Source Extractor works on both photographic plates and CCDs, and is used for the detection and photometry of sources in fits files.

The time corresponding to the peak magnitude (t^k_{peak}) was found for each image, k, by calculating the weighted mean of each light curve. The accuracy of this value with respect to the true peak (as seen in Fig. 3a) is of course a function of the number of observations made per field per filter (the observing strategy). We thus define the measured time delay (Δt^{1k}_{meas}) and its fractional error (δ^{1k}) for image k relative to image 1 to be:

$$\begin{aligned}\Delta t^{1k}_{meas} &= t^k_{peak} - t^1_{peak} \\ \delta^{1k} &= \frac{\Delta t^{1k}_{true} - \Delta t^{1k}_{meas}}{\Delta t^{1k}_{true}}\end{aligned} \qquad (1)$$

where Δt^{1k}_{true} are the true time delays (as given in Table 3) and the image number, $k = 2, 3, 4$.

---

[7] Using the *simlsst* code written by Masao Sako, SLAC.

2.4 Tests on System LSN

We wrote a script to execute the previously-described codes in a pipeline, where the output of one program provides the input for the next. The output of the pipeline is a set of light curves, one for each combination of field and filter. These light curves are then analysed to determine the time delay precisions (Eq. 1). The pipeline can be modified in future to study any arbitrary lens system, observed at any position in the sky. The description, inputs and outputs of each piece of code are summarised in Table 4. The pipeline was run twice, as described in §2.4.1 and §2.4.2.

Table 4: Summary of the programs used in the simulation pipeline.

Program	**Function**	**Inputs**	**Outputs**
1. *LSST cadence simulator*	Extract obs. dates	- LSST parameters - Run time	- Obs. dates per field - Filter used - Seeing - Sky brightness
2. *SIElens*	Model lens system	- Lens parameters - Source parameters	- Image separation - Image time delays - Magnification factors
3. *snlcsim*	Generate light curve	- Obs. dates per filter - Image time delays - Magnification factors	- Light curve per filter
4. *simlsst*	Simulate LSST images	- LSST parameters - Light curve per filter - Lens and source redshift - Seeing - Sky brightness	- Mock LSST image
5. *SExtractor*	Measure image flux	- Mock LSST image	- No. objects detected - Detected flux - Flux error
6. *tdelays*	Determine time delay	- Observation dates - Detected flux - Flux error	- Predicted time delay - Fractional error

2.4.1 Run 1 - Threshold source magnitude

We selected a single LSST field with a good visiting schedule, the light curve of which is shown in Fig. 3b). We artificially brightened the source by incrementing the magnitude by 0.5 on each loop (equivalent to shifting the light curve vertically upwards by this amount). This data was used to determine the threshold source peak-magnitude for good time delay measurements.

2.4.2 Run 2 - Field conditions and visiting schedule

For this run, System LSN was set to the threshold source peak-magnitude for good time delay measurements, as determined from Run 1. This System was placed in each LSST field, to investigate the following variables:

Field conditions: During good observation conditions, LSST is expected to image to magnitude 24 in two 15 second exposures. However, in practice, the minimum detectable magnitude will depend on the sky brightness and the seeing, and so the actual detection limit will vary about this value. The minimum detectable magnitude must be well below the threshold source peak-magnitudes to yield useful time delay measurements.

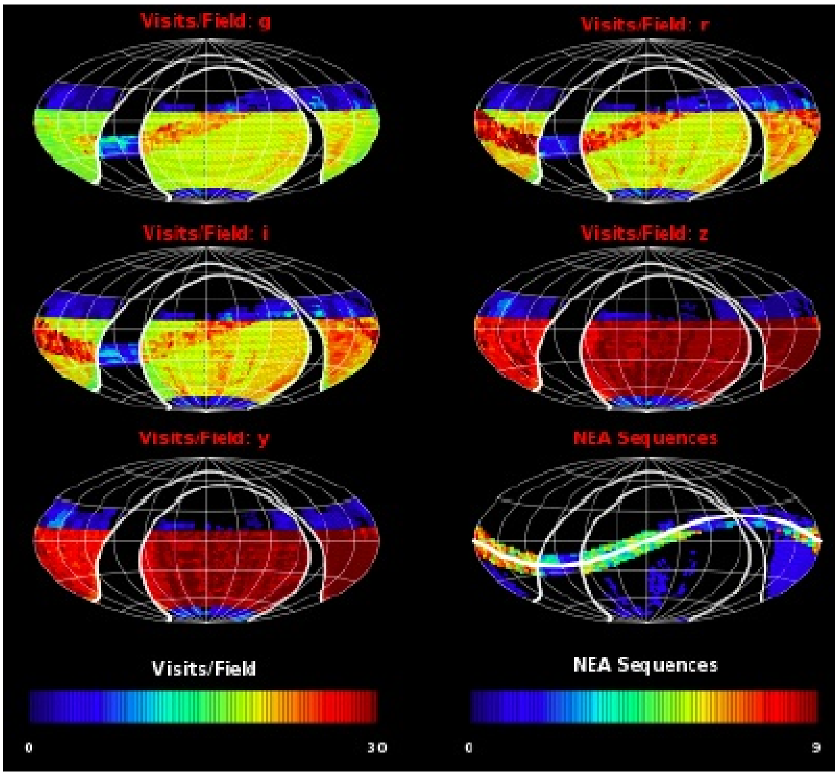

Figure 4: LSST annual sky coverage for Weak Lensing and Near Earth Asteroid (NEA) surveys, in each of the 5 filters (g, r, i, z, Y), and for the NEA survey alone. Red corresponds to the most frequent visits per field.

Visiting schedule: The LSST visiting schedule varies from field to field depending on its primary observation target [4]. Weak Lensing (WL) fields have a highly uneven cadence due to the requirements of the best possible seeing and minimum sky brightness. Such surveys require a minimum of $\sim$ 15, 15, 15, 25 and 25 observations per year in filters g, r, i, z and Y respectively. Filters z and Y are in the infra-red and far infra-red region (840 to 1030 nm). Measurements in these filters are used to reduce end effects, rather than to measure galaxy shapes. In addition, to reduce ellipticity systematics, WL observations must cover many telescope angles. Weak Lensing surveys thus span the entire visible sky. Near Earth Asteroid (NEA) fields require a completely different observing strategy: observations are limited to within 10° of the ecliptic plane, and usually two observations per night are required. These are separated by approximately half an hour, and taken on three nights per month. Figure 4 illustrates the WL and NEA visit schedules. These plots, extracted from the *LSST cadence Simulator*, depict the number of visits per field made in one year, for each filter. The ecliptic plane corresponds to the wavy band across the center of the plots; the Milky Way corresponds to the large “n-shaped” region where no observations are made. We see that WL sequences (the yellow and red regions) are distributed uniformly across the visible sky, and that all NEA sequences are made within the ecliptic plane.

We investigated the dependence of the precision on the time delays (between image pairs 1–2, 1–3 and 1–4) with this proposed LSST observing strategy.

3 Results and discussion

3.1 Run 1: Threshold source magnitude

The variation of fractional time delay error, δ^{1k}, as a function of the peak observed magnitude is summarised in Table 5. This data corresponds to a representative field condition and visiting schedule, which are the same for all measurements; only the peak observed magnitude is varied. In this way, the influence of the peak observed magnitude on the time delay error can be isolated. The untouched system, $\Delta_{mag} = 0$, corresponds to a peak magnitude in the range, 24.0–23.5. In this case, time delays between image pairs 1–2, 1–3 and 1–4 are measured to a precision of 27%, 36% and 12% respectively. The fractional error of the derived Hubble constant is equal to that of the time delay. Any one such measurement would therefore not improve our knowledge of H_0, which is currently measured to better than 10% precision. We see that a time delay precision below 10% is achieved when the peak observed magnitudes range from 22.5 to 22.0, or brighter. This corresponds to a magnitude offset relative to the original system (Table 2) of -1.5, i.e. a source magnitude of 24. Several thousand multiply-imaged supernovae with peak intrinsic magnitude of 24 or brighter are expected to be detected with LSST—however, these results show that the number that can be used to measure time delays to better than 10% will be significantly smaller. The threshold measured here will be used in estimating the size of this sub-sample, in future work. Nevertheless, we point out the high statistical precision available with even several hundred measurements of H_0, each at 10% precision.

Table 5: Variation of fractional time delay error, δ^{1k}, for image k relative to image 1, as a function of the peak observed magnitude. The same, representative, field condition and visiting schedule are used for all measurements; only the peak magnitude is varied.

Peak observed magnitude	**Magnitude shift Δ_{mag}**	**Time delay error, δ^{1k}**		
		$k = 2$	$k = 3$	$k = 4$
24.0–23.5	0.0	-.274	-.358	-.124
23.5–23.0	-0.5	-.210	-.152	-.078
23.0–22.5	-1.0	-.172	-.110	-.082
22.5–22.0	-1.5	-.092	-.099	.085
22.0–21.5	-2.0	.044	-.089	.043
21.5–21.0	-2.5	.017	-.010	-.035
21.0–20.5	-3.0	.017	-.005	-.025

3.2 Run 2: Field conditions and visiting schedule:

In this run, the influence of the field conditions and visiting schedule were investigated for each of the five filters, g, r, i, z and Y, as described below. Following the previous results, System LSN magnitude was set 1.5 brighter for Run 2, corresponding to a source magnitude of 24 and peak observed magnitudes 22.5–22.0.

3.2.1 Filter g (400–560 nm)

Field conditions: Figure 5 shows the dependence of the minimum detected magnitude as a function of seeing and sky brightness, in filter g. It shows that, under conditions of a dim sky background of 21 magnitude arcsec^{-2}, and relatively good seeing of 0.7 arcsec, LSST can image to 25 magnitude.

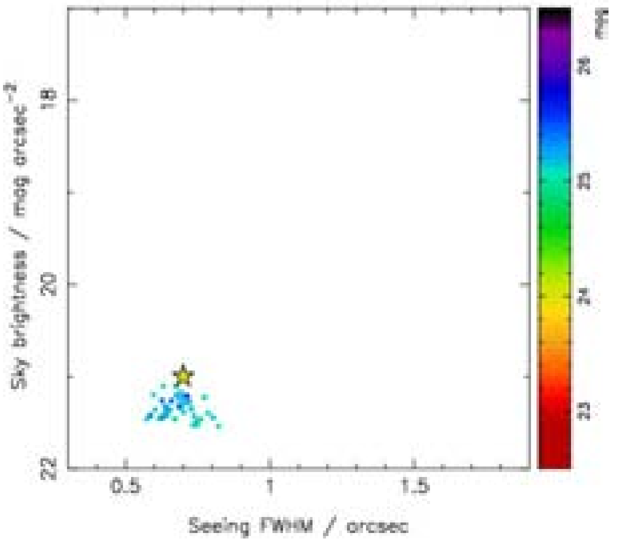

Figure 5: Minimum detected magnitude as a function of seeing and sky brightness, in filter g. Each data point represents one observation, in a particular field. The colour represents the minimum detected magnitude for that field. The star represents a standard reference point of seeing 0.7 arcsec and sky brightness 21 magnitude arcsec^{-2}.

Visiting schedule: Despite the good conditions and high minimum observed magnitude, this filter did not yield any time delay measurements. We found that the maximum number of observations per field never exceeded five, and measurements were only ever made of one out of the four images. This was probably because all observations were taken over a short span of days, during which only one of the four images was sufficiently bright. Thus, no time delay between images could be measured. The small number of observations is a direct consequence of the small number of visits per field with filter g, for the nominal LSST visiting schedule. Since the g filter (400–560 nm) is not optimised for large redshift sources, it is, in any event, not central to the strong lensing program.

3.2.2 Filter r (540-720 nm)

Field conditions: Figure 6 shows the dependence of the minimum detected magnitude as a function of seeing and sky brightness, in filter r. We see that the minimum detected magnitude improves with better (smaller) seeing, as expected. All fields include observations on days where the sky brightness has a low value, between about 20.8 to 21.5 mag. On days where the seeing is less than 1 arcsec, LSST can image typically to 24.5 magnitude, or better. Since this is well below the peak threshold magnitude of 22, the supernova light curves should be well measured. At poorer seeings, above about 1 arcsec, the magnitude limit is greater than 24.5. However, only a small fraction of the observations have poor seeing values.

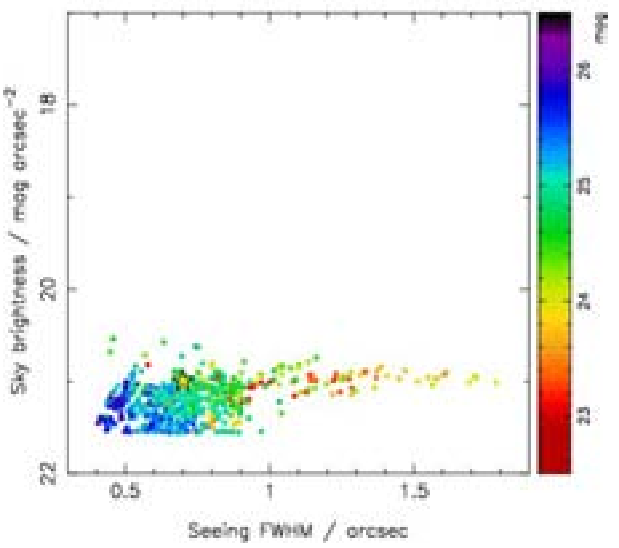

Figure 6: Minimum detected magnitude as a function of seeing and sky brightness, in filter r (Fig. 5 caption provides more detail).

Visiting schedule: Panels a) in Figs. 7–9 show histograms of the fractional time delay error, δ^{1k} (Eq. 1), between the image pairs 1–2, 1–3 and 1–4 respectively. The variation of the error with number of visit days per field and number of detections is shown in panels b) of these figures. The large number of data points in panels b) indicate a high frequency of visits with filter r. The histograms show a peak centered about zero, which corresponds to good time delay measurements. Poorer measurements are indicated by the additional peaks: common to image pairs 1–2 (Fig. 7) and 1–3 (Fig. 8) is a secondary peak at a value of 1; image pair 1–2 has a tertiary peak at a value of -0.7. In panels b), we see that the number of detections increases linearly with number of days, as expected, reaching a maximum of approximately 120 detections for 150 days of observation. The reduced number of detections is the result of poor observation conditions. The general trend is that the time delay error improves with increasing number of detections. This is discussed further in the following section.

Discussion: We find that the r filter provides the best time delay measurements, and as such constitutes the main search filter. It is the principal filter for the weak lensing dataset, due to the low sky brightness, which leads to high numbers of visible faint galaxies. In addition, images taken with this filter have the smallest level of image contamination from internal reflections and diffraction effects in the telescope optics. The weak lensing science therefore dictates r-filter use when conditions allow—implying frequent, all-sky coverage. For our purposes, the extended red acceptance of the r filter is well matched to supernovae spectra. Together, these are ideal conditions for time delay measurements of lensed supernovae.

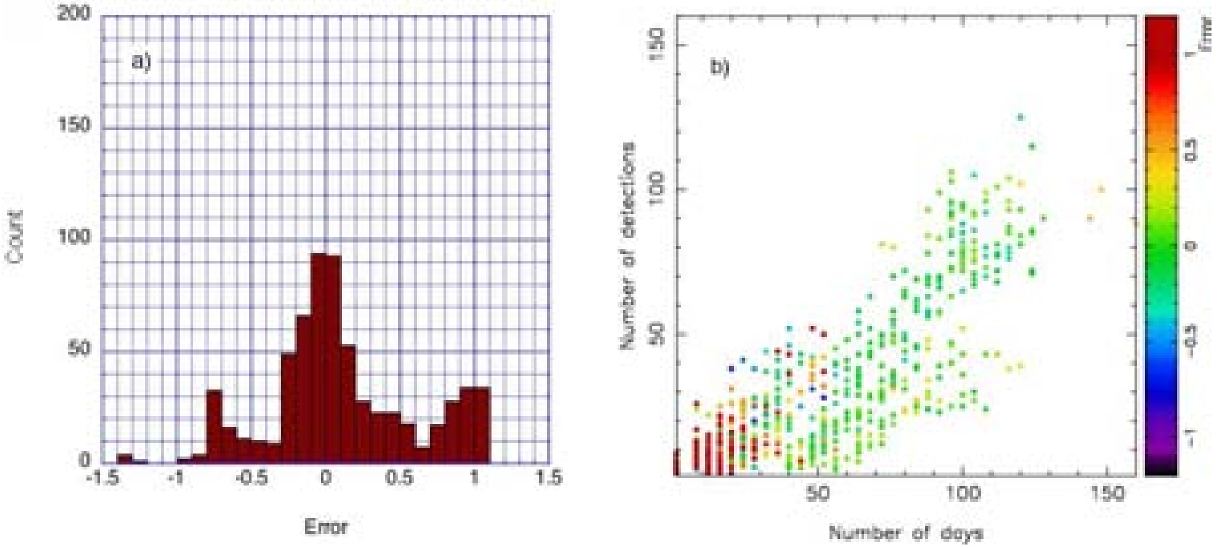

Figure 7: Measurements of image pair 1–2 with filter r: a) fractional error distribution, and b) number of visit days per field vs. number of detections made. In panel b), the colour of each data point indicates the fractional error obtained in that field.

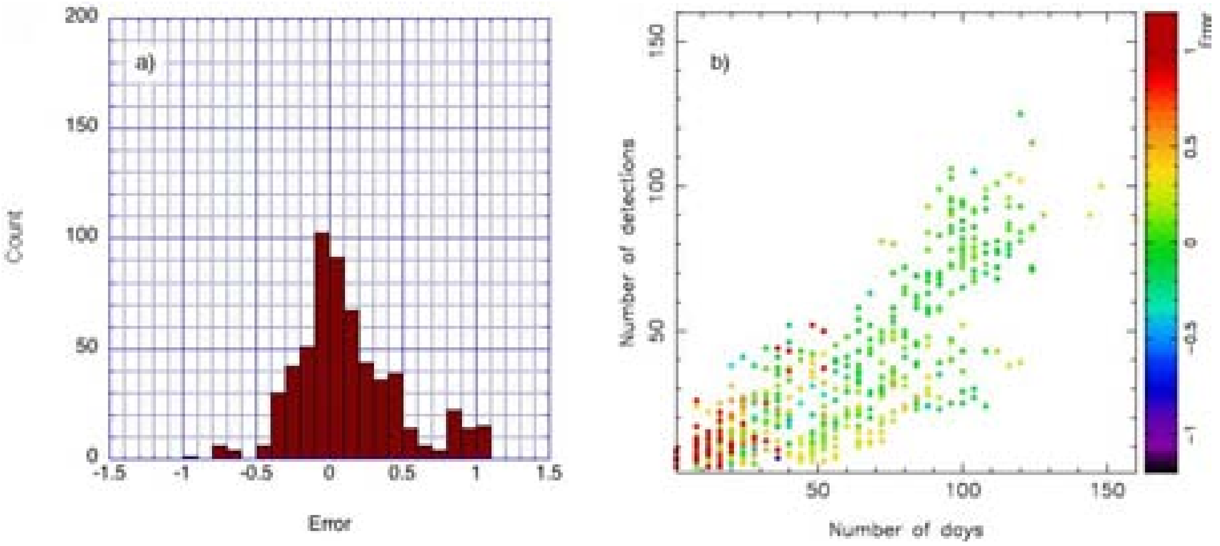

Figure 8: Measurements of image pair 1–3 with filter r: a) fractional error distribution, and b) number of visit days per field vs. number of detections made. In panel b), the colour of each data point indicates the fractional error obtained in that field.

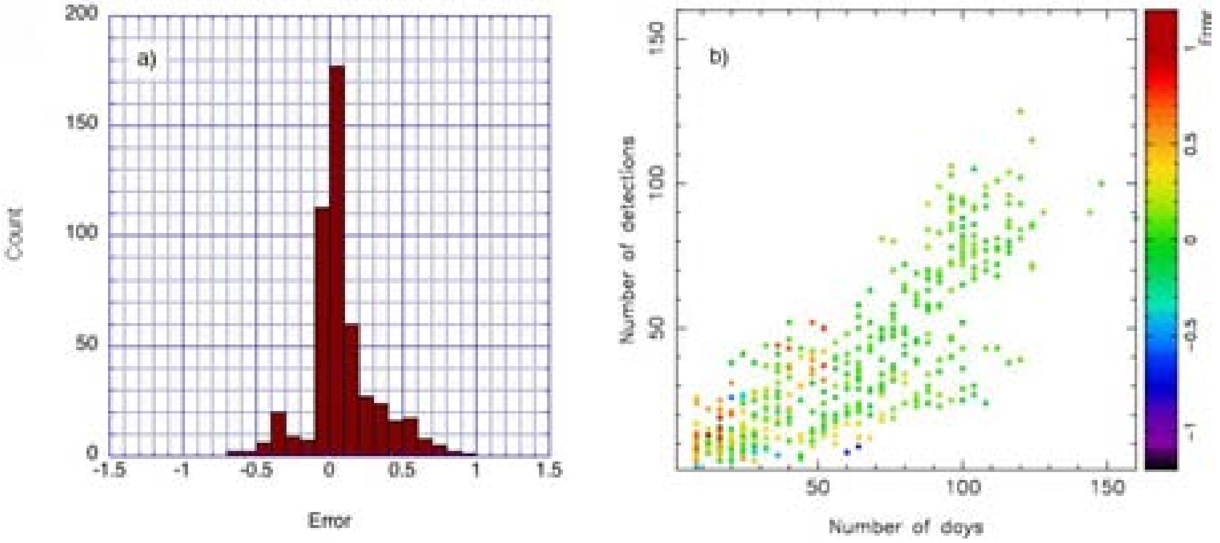

Figure 9: Measurements of image pair 1–4 with filter r: a) fractional error distribution, and b) number of visit days per field vs. number of detections made. In panel b), the colour of each data point indicates the fractional error obtained in that field.

The central peak seen in panels a) results from fields that have a large number of visit days, and hence a large number of detections. Examples of corresponding light curves are shown in Fig. 10. With the observed sampling interval of about 10–15 days, the time-development of the four images is clearly resolved. Image pair 1–4 (indicated by the black and red curves in Fig. 10) has the longest time delay, thus the fractional errors are smaller than for the other two image pairs. The histogram for image pair 1–4 (Fig. 9a) therefore has the narrowest full-width half-maximum. Good measurements correspond to a time delay measurement error below 10% (Fig. 9a). The necessary conditions are at least about 50 visit days per field (as seen in Fig. 9b), spaced regularly over the observation period so that the curves are well sampled.

The peak at 1, seen for image pairs 1–2 (Fig. 7a) and 1–3 (Fig. 8a), corresponds to a measured time delay of zero (Eq. 1). These measurements occur in fields that have fewer than about 20 visit days, as indicated by the red data points in Figs. 7b) and 8b). Illustrative light curves are shown in Fig. 11. The small number of detections frequently occurs within a short time period, thus all images appear to peak on the same day, leading to a time delay measurement of zero. These poorly-measured delays can easily be eliminated by applying a minimum quality cut on the data. The absence of a peak at 1 in Fig. 9a) is an artefact of the visit schedule: observations fall on days where image 4 (red curve) has zero flux.

The tertiary peak at -0.7 in Fig. 7 is also an artefact of the visit schedule. Examples are shown in Fig. 12. In this class of measurements, there are two predominant observations, separated by an interval of approximately 55 days. The three image pairs thus appear to have the same time delay of about 55 days. This leads to time delay errors of about -0.7, -0.3 and 0 between image pairs 1–2, 1–3 and 1–4, respectively.

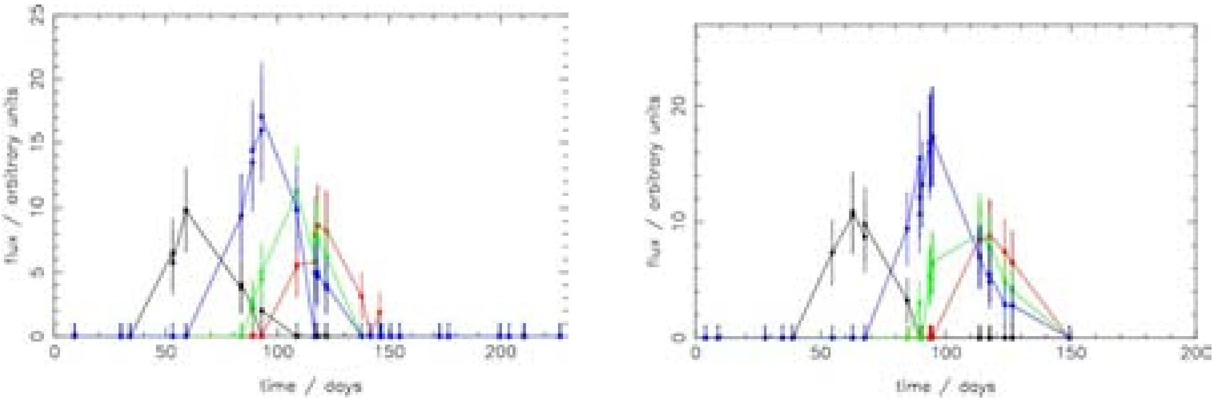

Figure 10: Two examples of measured light curves corresponding to good time delay measurements, with filter r. The four coloured curves correspond to the four lensed images (as in Fig. 3).

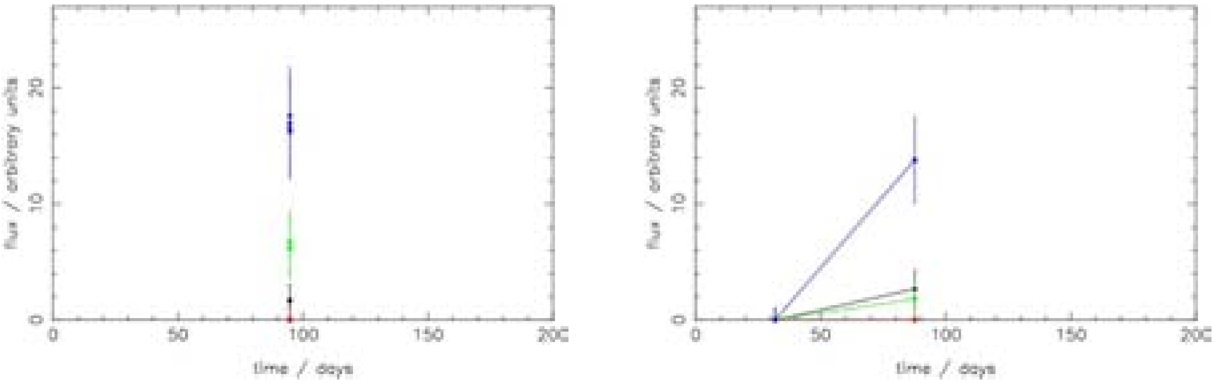

Figure 11: Two examples of poorly-sampled light curves, which result in apparent time delays of zero (filter r).

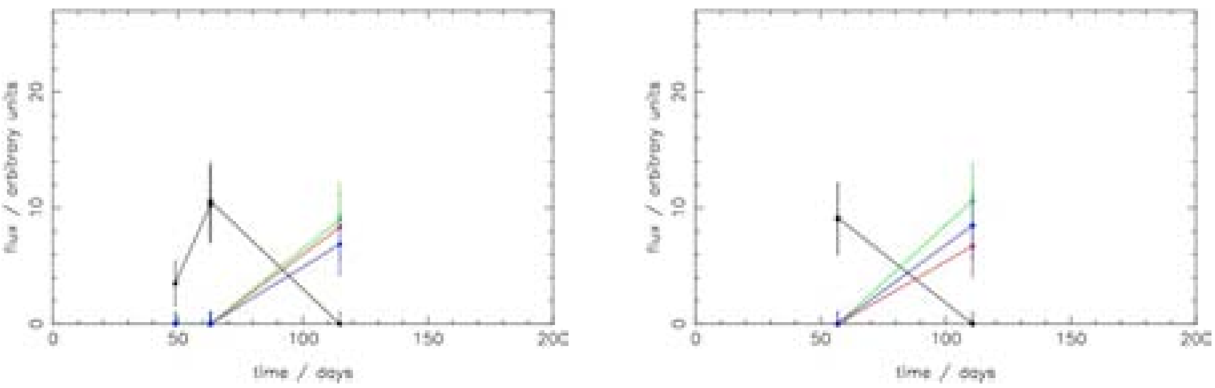

Figure 12: Two examples of poorly-sampled light curves, which result in apparent time delays of about 55 days (filter r).

3.2.3 Filter i (685-870 nm)

Field conditions: Figure 13 shows the dependence of the minimum detected magnitude as a function of seeing and sky brightness, in filter i. For this filter, the fields always involve days where the sky brightness is dimmer than about 20 magnitude arcsec^{-2}, and the seeing is less that about 1 arcsec. Under these conditions, LSST images to magnitude 24 in almost all fields.

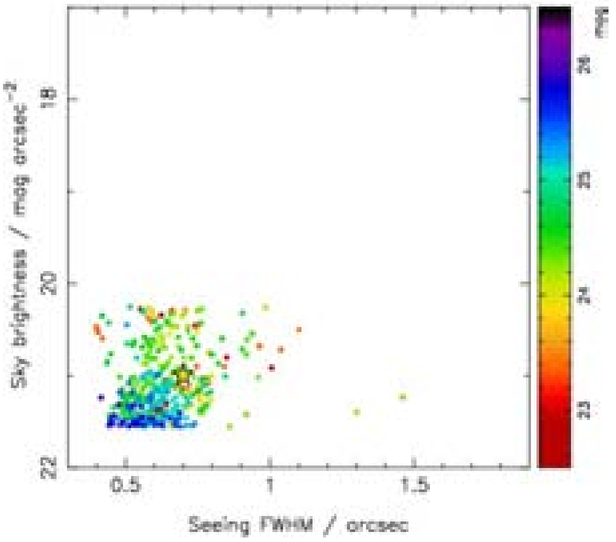

Figure 13: Minimum detected magnitude as a function of seeing and sky brightness, in filter i (Fig. 5 caption provides more detail).

Visiting schedule: Panels a) in Figs. 14–16 show histograms of the fractional time delay error, δ^{1k} (Eq. 1), between the image pairs 1–2, 1–3 and 1–4 respectively. The variation of the error with number of visit days per field and number of detections is shown in panels b) of these figures. In contrast to the r filter histograms (Figs. 7a–9a), there are no longer clearly defined peaks centered about zero. The three histograms share the following two characteristics: a sharp, narrow peak at 1, and a broader, off-zero peak. This second feature suggests that the measured time delay is systematically shorter than the true time delay. There are few fields with greater than 50 observation days (Figs. 14b–16b), which, for the present analysis, marks the minimum required for good time delay measurements. (Improvements in the analysis will be discussed later.) Moreover, the sky brightness is somewhat higher for this filter than for filter r (compare Figs. 6 and 13).

Discussion: The reason for the peak at 1 in Figs. 14a–16a has been previously described in §3.2.2. The frequency of this occurrence is high since the majority of fields have a small number of observation days. Examples of light curves producing the systematic off-zero peak are shown are Fig. 17. These cases are due to a sparse sampling of around three measurements, with time intervals of about 20 days. These measurements systematically miss the image peaks, and create apparent equal time delays for the image pairs, leading to time delay errors of about 0.3, 0.4 and 0.5 between image pairs 1–2, 1–3 and 1–4, respectively. As before, these poorly-measured delays can be readily eliminated by applying a minimum quality cut on the data. In summary, therefore, this filter is not useful for time delay measurements, primarily due to the sparse visiting schedule.

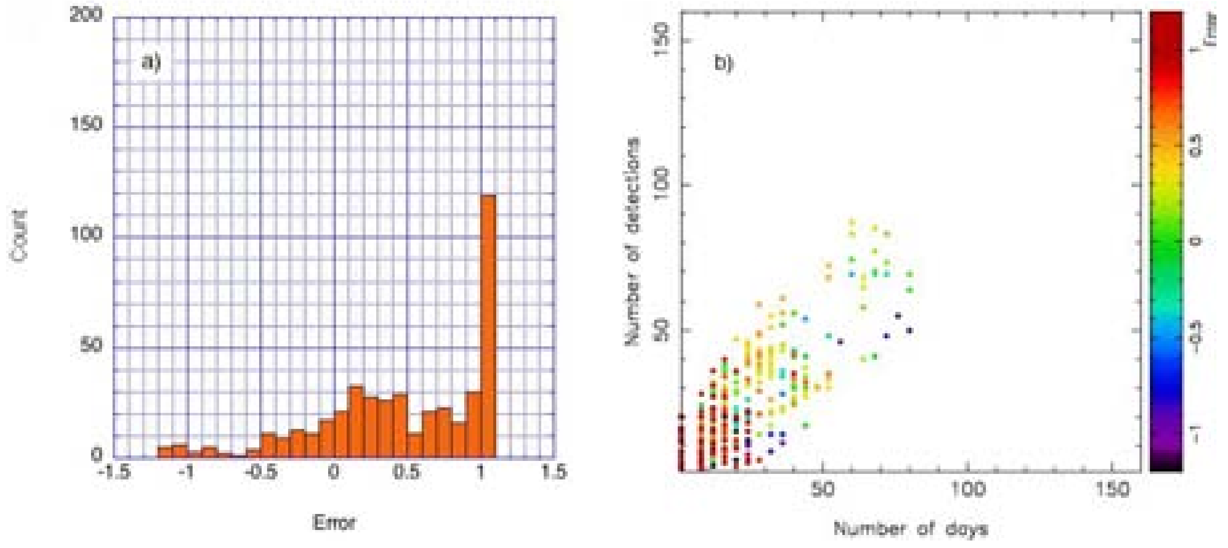

Figure 14: Measurements of image pair 1–2 with filter i: a) fractional error distribution, and b) number of visit days per field vs. number of detections made. In panel b), the colour of each data point indicates the fractional error obtained in that field.

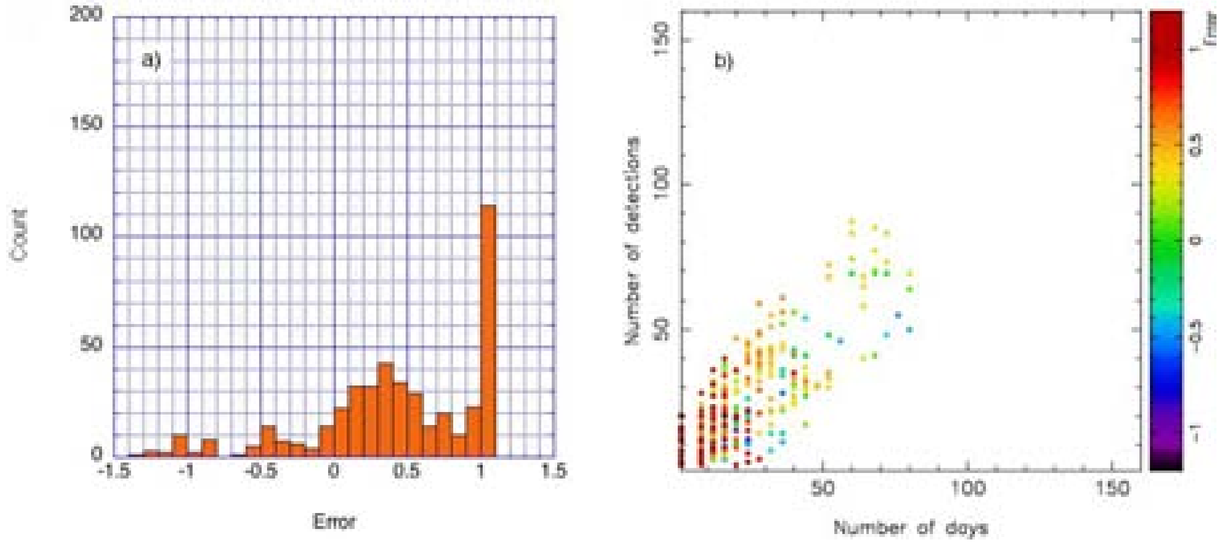

Figure 15: Measurements of image pair 1–3 with filter i: a) fractional error distribution, and b) number of visit days per field vs. number of detections made. In panel b), the colour of each data point indicates the fractional error obtained in that field.

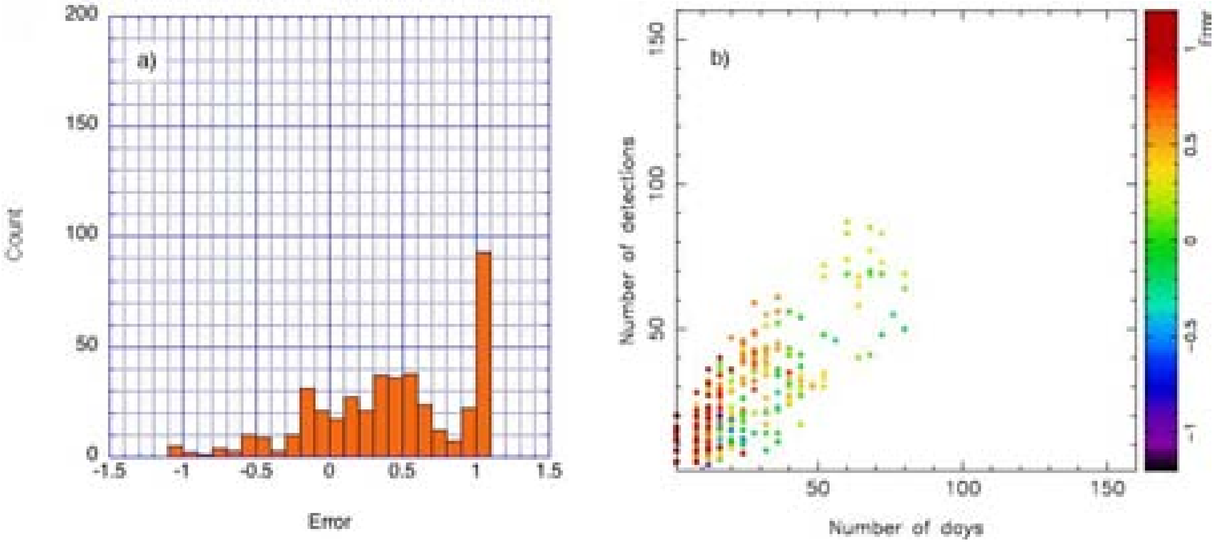

Figure 16: Measurements of image pair 1–4 with filter i: a) fractional error distribution, and b) number of visit days per field vs. number of detections made. In panel b), the colour of each data point indicates the fractional error obtained in that field.

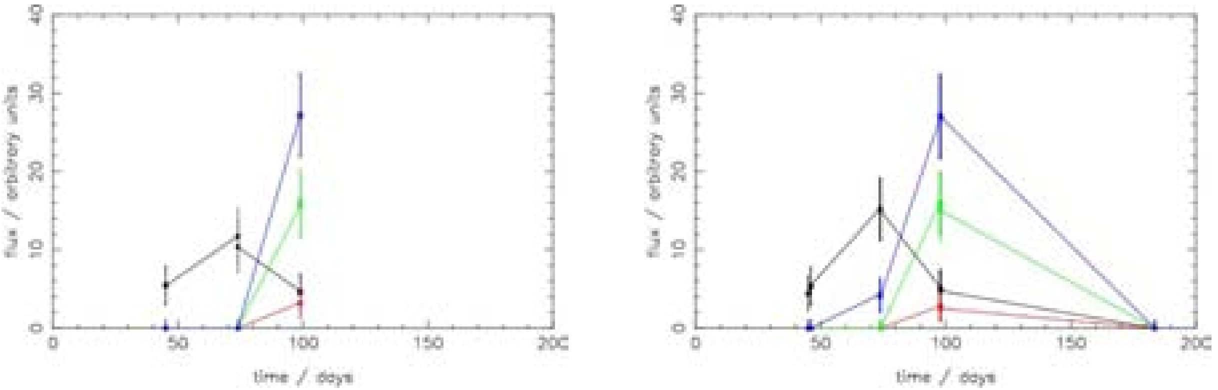

Figure 17: Two examples of poorly-sampled light curves with filter i, which result in apparent time delays of about 25–30 days.

3.2.4 Filter z (840-950 nm)

Field conditions: Figure 18 shows the dependence of the minimum detected magnitude as a function of seeing and sky brightness, in filter z. There is a much larger scatter of data points compared with Figs. 5, 6 and 13, which are the corresponding plots for the g, r and i filters respectively. Observations in filter z are no longer limited to a dim sky brightness; the range extends over 3 magnitudes, from about 21 to 18 magnitude arcsec^{-2}. In addition, there is a large range of seeing, from about 0.5 to 1.3 arcsec. The sharp cut-off at 1.3 arcsec suggests that LSST will not schedule observations in this filter if the seeing exceeds this value. Under these conditions, LSST can image only to magnitudes of between about 24.5 and 23, requiring significantly brighter sources than those for filters g, r and i.

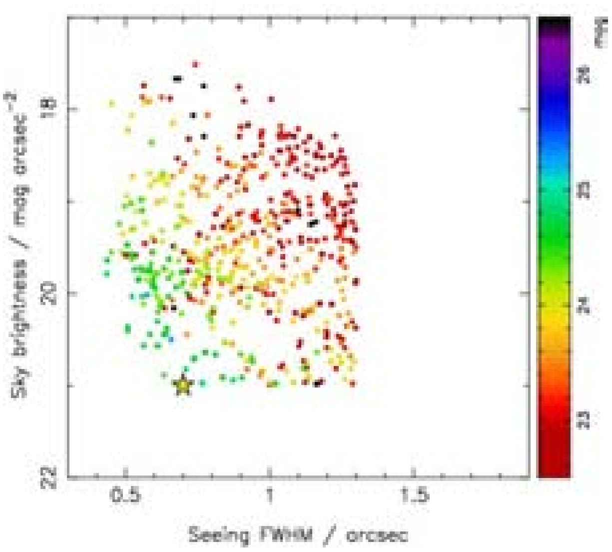

Figure 18: Minimum detected magnitude as a function of seeing and sky brightness, in filter z (Fig. 5 caption provides more detail).

Visiting schedule: Panels a) in Figs. 19–21 show histograms of the fractional time delay error, δ^{1k}, between the image pairs 1–2, 1–3 and 1–4 respectively. The variation of the error with number of visit days per field and number of detections is shown in panels b) of these figures. The visit schedule is typically below 50 days per field, and is similar to filter i (Figs. 14b–16b). This leads to error histograms with similar characteristics to those for filter i, with a broad peak centered on positive values.

Discussion: As before, filter z is not useful for time delay measurements, primarily due to the sparse visiting schedule.

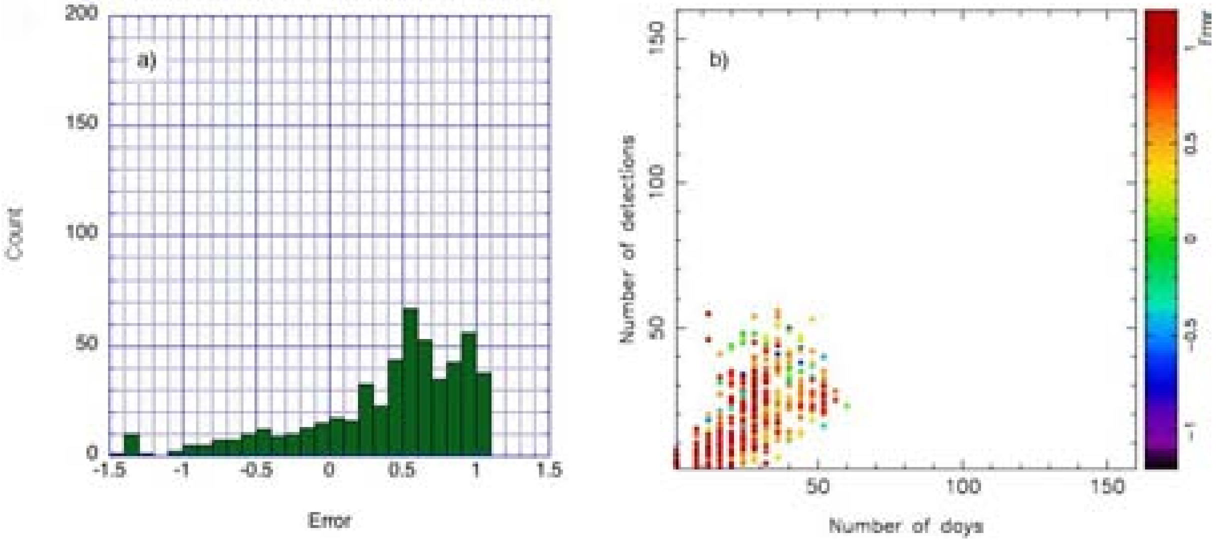

Figure 19: Measurements of image pair 1–2 with filter z: a) fractional error distribution, and b) number of visit days per field vs. number of detections made. In panel b), the colour of each data point indicates the fractional error obtained in that field.

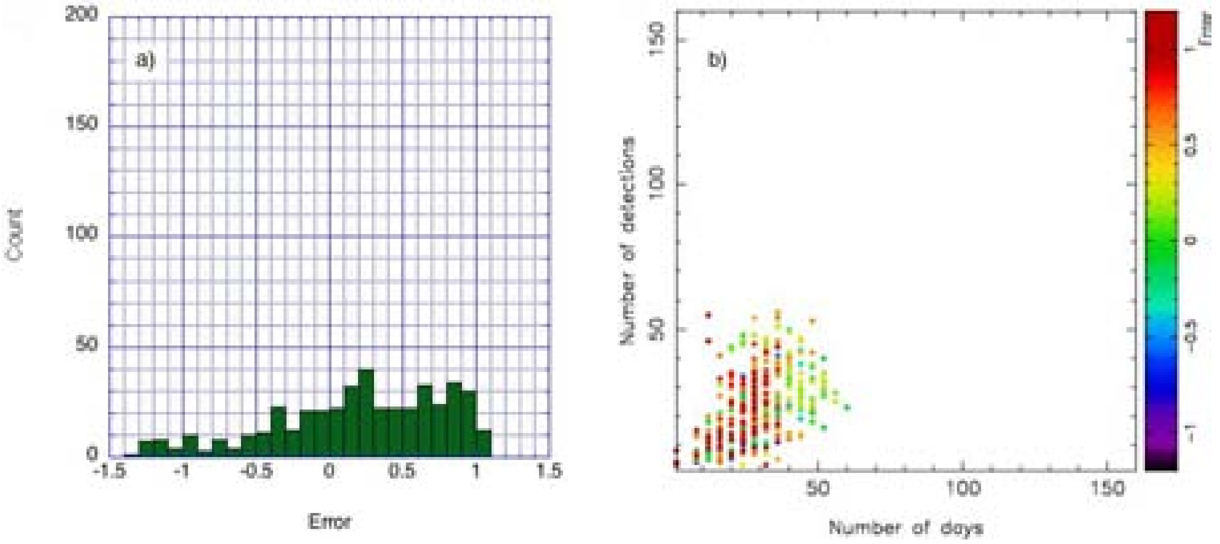

Figure 20: Measurements of image pair 1–3 with filter z: a) fractional error distribution, and b) number of visit days per field vs. number of detections made. In panel b), the colour of each data point indicates the fractional error obtained in that field.

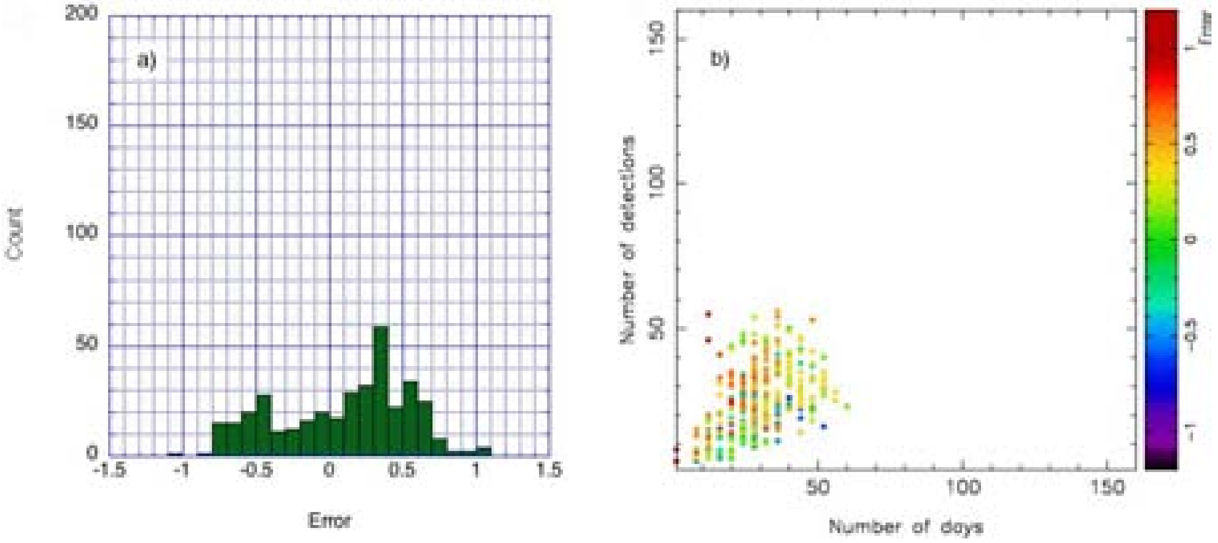

Figure 21: Measurements of image pair 1–4 with filter z: a) fractional error distribution, and b) number of visit days per field vs. number of detections made. In panel b), the colour of each data point indicates the fractional error obtained in that field.

3.2.5 Filter Y (945-1030 nm)

Field conditions: Figure 22 shows the dependence of the minimum detected magnitude as a function of seeing and sky brightness, in filter Y, the far infra-red filter. As with the z filter, observations range over a sky brightness of 21 to 18 magnitude arcsec^{-2}. Here, the seeing threshold appears to be 1 arcsec, in contrast with 1.3 arcsec for filter z. Measurements range from a minimum magnitude of about 25, when conditions are best (seeing about 0.5 arcsec, sky brightness about 21 magnitude arcsec^{-2}), to a maximum of about 23.

Visiting schedule: Panels a) in Figs. 23–25 show histograms of the fractional time delay error, δ^{1k}, between the image pairs 1–2, 1–3 and 1–4 respectively. The variation of the error with number of visit days per field and number of detections is shown in panels b) of these figures. The visit schedule is typically below 50 days per field, which results in histograms that display similar characteristics as for filters i and z.

Discussion: The same conclusion is obtained as for the previous two filters, namely that filter Y is unsuitable for time delay measurements, owing to the sparse visiting schedule.

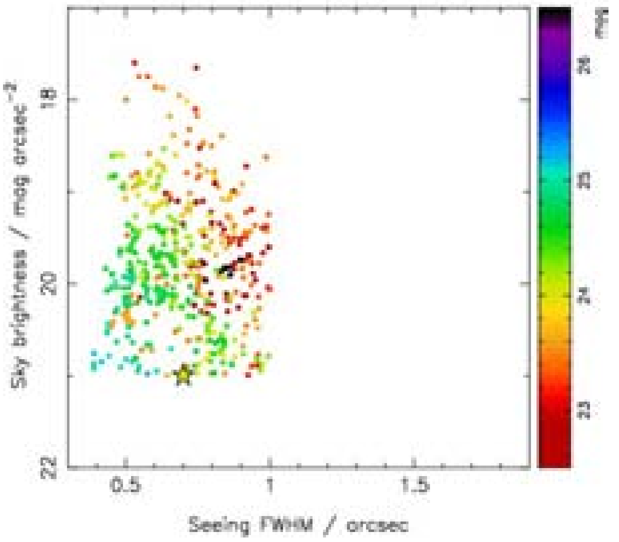

Figure 22: Minimum detected magnitude as a function of seeing and sky brightness, in filter Y (Fig. 5 caption provides more detail).

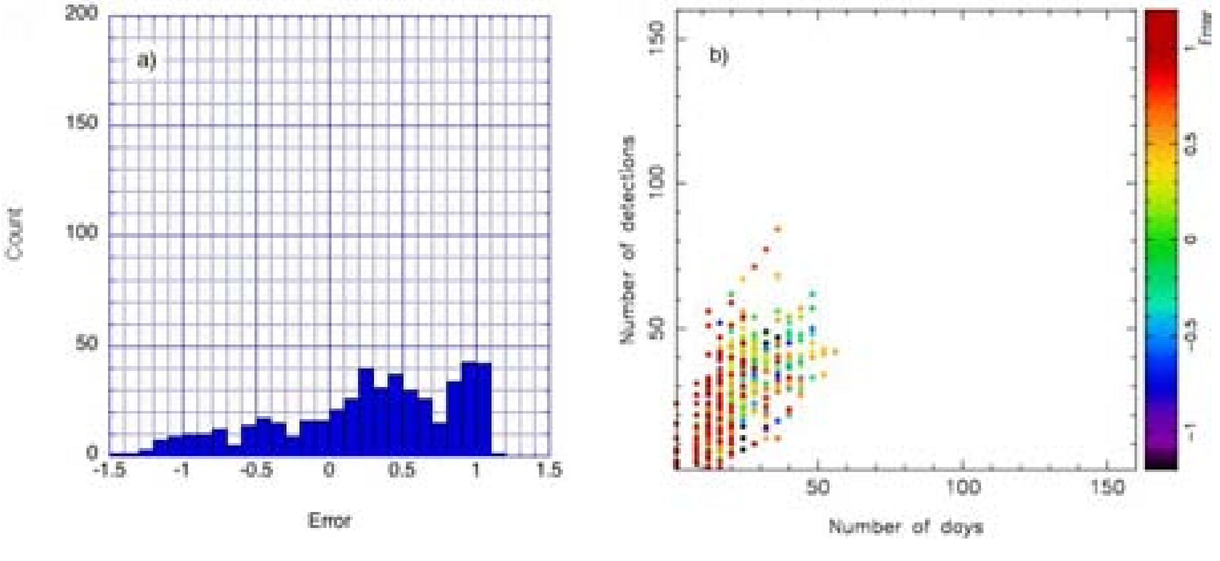

Figure 23: Measurements of image pair 1–2 with filter Y: a) fractional error distribution, and b) number of visit days per field vs. number of detections made. In panel b), the colour of each data point indicates the fractional error obtained in that field.

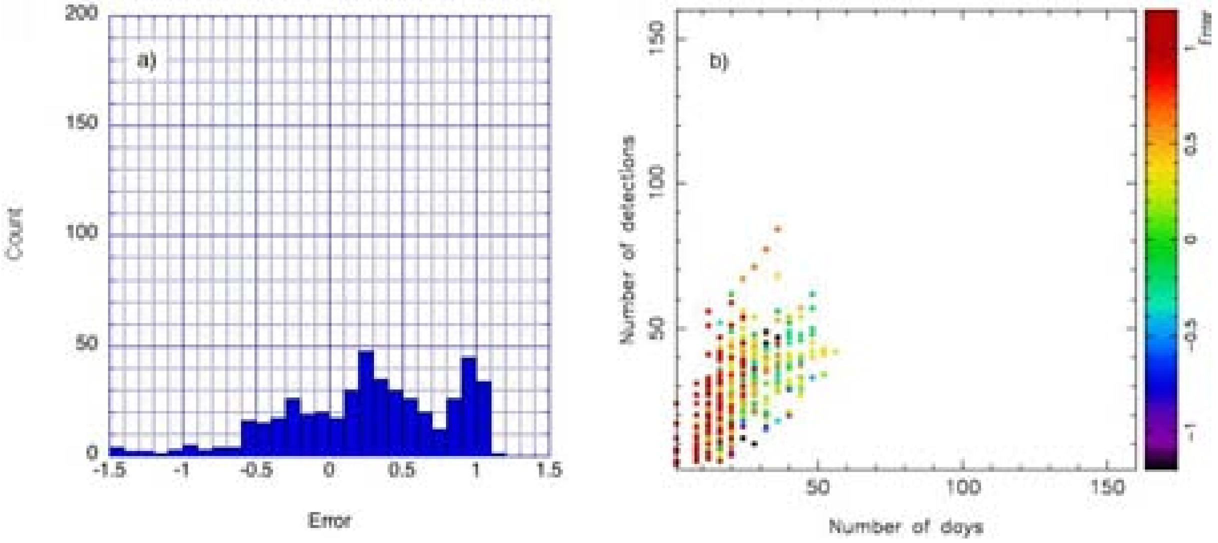

Figure 24: Measurements of image pair 1–3 with filter Y: a) fractional error distribution, and b) number of visit days per field vs. number of detections made. In panel b), the colour of each data point indicates the fractional error obtained in that field.

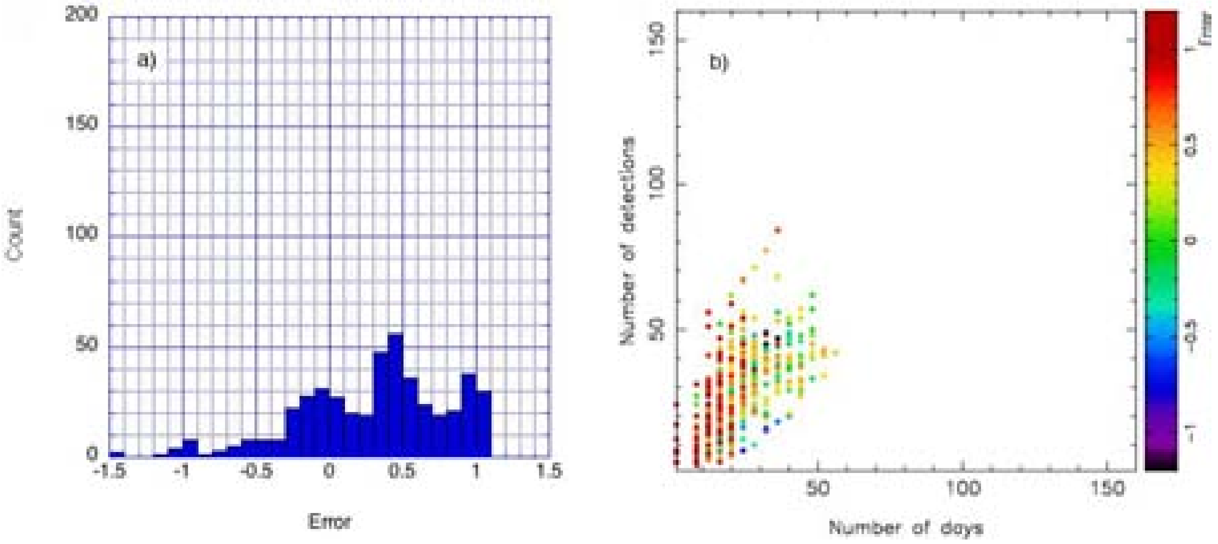

Figure 25: Measurements of image pair 1–4 with filter Y: a) fractional error distribution, and b) number of visit days per field vs. number of detections made. In panel b), the colour of each data point indicates the fractional error obtained in that field.

4 Conclusions

LSST can measure gravitational lens time delays to better than 10% precision per image-pair, under the following conditions:

1. **Threshold source peak-magnitude:** A minimum peak observed magnitude of about 22.5–22.0 is required. For typical galaxy-scale lenses providing magnifications of around 10, this corresponds to an intrinsic source magnitude of 24–25. The expected number of lensed supernovae visible with LSST is under investigation; the magnitude threshold measured here is a key ingredient of this calculation.

2. **Visiting schedule:** A minimum of about 50 visit days per field is required for a lensed Type Ia supernova. These visits must be evenly distributed over the duration of the event; the minimum visit frequency should be once approximately every 10–15 days. With the nominal LSST observing strategy, we find about 15% of all fields exceed 50 visit days: 13% in the r filter alone and 2% in all remaining filters combined. The r filter, with its high visit frequency and good spectral acceptance, provides ideal conditions for precise time delay measurements. Fig. 26 shows the fractional error distribution of these fields, integrated over all filters. The central peak indicates a time delay measurement precision, $\sigma = 0.12$.

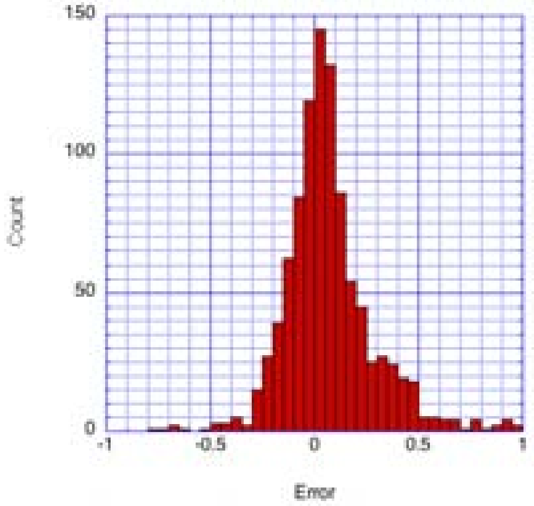

Figure 26: Fractional time delay error distribution for fields exceeding 50 visit days, for any filter. A Gaussian fit to the central peak gives $\sigma = 0.12$ and $\mu = -0.001$.

3. **Field conditions:** At a sky brightness of 21 magnitude arecsec^{-2}, the LSST images permit point-source detections down to a magnitude limit of about 24.5 in 30 seconds exposure time. This fiducial limit is well below the threshold peak-magnitude of about 22 and so will allow good light curve measurements. The resolution of the lensed images will directly depend on the seeing. For the representative System LSN, a seeing of better than about 1 arcsec is required. For the proposed locations of LSST, the seeing is typically better than this value. Good seeing will also improve the sensitivity to weaker supernovae (those at greater distances).

The primary conclusion from this study is that the visiting schedule is the single most important parameter to optimise for time delay measurements. The proposed LSST schedule results in a visiting frequency of typically 20 to 30 days per field, over the duration of the supernova event. This is inadequate for precision measurements. An alert system is therefore required and, once the supernova has been detected, frequent regular observations can be made. Cadences of approximately one week appear sufficient for high precision time delay measurements.

Significant improvements can also be made in the analysis. In particular, for this study the time delays were evaluated on the simple basis of weighted means of the light curves. The next step is to fit the measurements to the predicted supernovae light curves, once the type is known. This will improve the sensitivity to weaker systems and allow for sparse time sampling.

In summary, the proposed design and visiting schedule of the LSST should provide a large sample of precision gravitational lens time delay measurements—and significant improvements can be made with further optimisation.

Acknowledgments

It is a pleasure to thank Marusa Bradac, Stuart Marshall, Liz Rivers, Masao Sako and, in particular, my supervisor Phil Marshall for their guidance and for many enjoyable and stimulating discussions. I would also like to express my appreciation to Helen and Dan Quinn, James Lindesay and my fellow SULI colleagues for their warm friendship and hospitality during my visit to SLAC. Finally, I would like to thank the the U.S. Department of Energy, Office of Science for creating, organising, and funding the SULI program, which made this work possible. This work was supported in part by the U.S. Department of Energy under contract number DE-AC02-76SF00515.

References

[1] LSST homepage: http://www.lsst.org

[2] Marusa Bradac, *Substructure in the Gravitationally Lensed System B1422+231*, Bonn, Germany (2001).

[3] Cerro Tololo Inter-American Observatory homepage: http://www.ctio.noao.edu

[4] Dark Energy Task Force Committee, Rocky Kolb (chair), *The Large Synoptic Survey Telescope*, (2004).

[5] E. Bertin and S. Arnouts, *SExtractor: Software for source extraction*, (1996).